Simulation of $CaCO_3$ reverse osmosis membrane scaling at a continuously increasing scaling propensity

Abraham Sagiv, Raphael Semiat, Hilla Shemer*

Rabin Desalination Laboratory, Department of Chemical Engineering, Technion-Israel Institute of Technology, Haifa 3200003, Israel, Tel.: +97248295047; email: shilla@technion.ac.il (H. Shemer)

ABSTRACT

The development of calcium carbonate scale on the surface of a reverse osmosis membrane under continuously increasing scaling propensity conditions obtained by recycling the concentrate back to the feed tank in the presence of antiscalants is presented. The work combines experimental results and modeling based on computational fluid dynamics simulation. The model accounts for two distinct flux decline regimes: one due to continuously increasing osmotic pressure, which resulting from permeate withdrawal, and the other due to scale-mass growth. These two regimes are separated by the onset of scaling (OS), indicated by the observed sharp permeate flux decline. The experimental data were well replicated, revealing the water recovery fraction at the OS and the permeate flux profile as a function of the water recovery. The model fit the experimental data well, yielding a pair of adjustable parameters: the deposition rate coefficient and the water recovery fraction at the onset of scaling. With these two adjustable parameters, the model provides concentration profiles of calcium in the bulk solution and on the membrane surface. The model also provides the membrane surface coverage fraction. Overall, the model provides a quantitative approach for simulating scale development and determining the onset of scaling under different desalination conditions.

Keywords: Precipitation; Crystallization; Computational fluid dynamics; Desalination; Scale deposition

1. Introduction

Membrane scaling of sparingly soluble salts such as calcium carbonate, calcium sulfate, and silica is an inherent process of desalination. Mineral scaling reduces the permeate flux, increases operational cost, and shortens the membrane's lifespan [1–4]. The economic impact of scaling on desalination processes requires understanding of its sources, causes, effects, and control methods. From this aspect, to minimize the costs, it is necessary to maximize the production time until the onset of scaling. This goal motivates decades of experimental and theoretical research into scaling mechanisms and their impact on the onset of scaling (OS). A key issue in reverse osmosis (RO) membrane scaling is the adequacy and reliability of available methods for assessing feedwater scaling propensity, selecting and optimizing scaling control schemes, and monitoring membrane scale-formation during plant operation [5].

When the solubility limits of sparingly soluble salts are exceeded, a scale layer tends to precipitate on the membrane. The precipitation occurs with salt nuclei formed directly on the membrane surface or in the bulk solution. On the membrane surface, nuclei grow with increasing concentration polarization (CP) and the related supersaturation [5–7].

The key mechanisms and factors governing membrane scaling include membrane properties such as surface roughness, charge, and functionality, as well as feed water quality parameters like pH, temperature, and ionic strength. High crossflow hydrodynamics can minimize the CP of

---

* Corresponding author.

scale-inducing ions adjacent to the membrane surface and, thus, reducing surface nucleation. Feed flow and permeation flux significantly impact nucleation, nuclei attachment and detachment due to shear forces, and surface crystal growth. To optimize operational conditions and membrane system configurations, an understanding of nucleation kinetics, including induction time and flux decline, is important [2,3,8].

Real-time surface imaging based on the detection of micron-sized crystals by analytical empirical techniques such as Raman microscopy, scanning electron microscopy, and optical imaging, is used for monitoring membrane scaling. A detailed description of these methods is given by Karabelas et al. [5]. It should be realized that pressure vessels are characterized by uneven flux, which makes some tail-end membranes more susceptible to scaling than others [9]. In addition, the small particles conveyed by the feed stream had no impact on the total deposit mass flux [10].

There are several methods employed to mitigate scaling in industrial systems, including removing scaling species from the feed, adjusting the feed pH, and extending the effective solubility limits of scaling salts by the dosage of antiscalants. In the latter, the mechanisms that contribute to scale suppression are crystal distortion and surface charge effects that hamper adhesion of the scale deposit onto a flow surface. The quantitative aspects of the inhibition mechanisms are lacking, and the effects of operating parameters on inhibition effectiveness are largely unpredictable and require experimentation. One methods for determining the relative effectiveness of antiscalant is the concentrate recycle technique. In this technique, permeate is withdrawn from the system and the concentrate is recycled back to the feed tank, leading to continuous concentration of the recycling solution [11–13]. In this technique, the upper scaling threshold limit, that is, the concentration level at which the supersaturation level reached by the concentrate triggers an immediate precipitation, is detected by a rapid drop in membrane flux permeability. The advantages of this technique are that it can be undertaken at a relatively short experimental time, lasting only a few hours, and that the system operates under hydrodynamic conditions simulating the Reynolds number and geometry of the industrial module. The residence time of the concentrate in the RO module is much shorter than that prevailing in the concentrate recycle tests; hence, it is conceivable that a long residence time might accelerate nucleation processes and enhance scaling tendencies. Nonetheless, tests comparing permeability declines in once-through and concentrate recycle systems yielded similar results [14,15].

Two-dimensional (2D) and three-dimensional (3D) models have been developed to simulate flows in RO modules using computational fluid dynamics (CFD) tools. These simulations mainly focus on the flow behavior of the feed spacers [9]. Models developed to evaluate scaling rely on empirical correlation of the scale-mass deposition rate and the supersaturation ratio [16], and theories of crystallization and resistance-in-series [8]. Others use the lattice Boltzmann method, coupled with the measurement of supersaturation near the membrane, to predict the concentration polarization and scaling growth on the membrane surface at a single crystal level [17]. A two-dimensional mathematical model

integrating fluid flow and solute mass transport with a particle-based approach for crystal nucleation and growth enables the description of the permeate flux decline or increase of the transmembrane pressure [18]. A method for evaluating the induction time of gypsum scaling, based in CFD simulations was recently proposed [10]. The gypsum scaling of each RO element in a full-size six-element pressure vessel treating coal mine water was simulated and predicted using a 3D numerical model. Parametric simulations were used to enable the prediction of gypsum scaling under various operating conditions, including feed pressure, flow rate, feed total dissolved solids (TDS) concentrations, and calcium sulfate concentrations [19].

Much research effort has been put into understanding the mechanism of scale formation and its mitigation. These efforts have led to the development of experimental and theoretical methods aimed at maximizing desalinated water production and scale mitigation. The objective of this study was to develop a 2D-CFD model to simulate calcium carbonate scaling of RO membranes under conditions of continuously increasing scaling propensity. The model relies on the results of pilot-scale RO concentrate recycling experiments.

2. Experimental set-up

2.1. Experimental system

Experiments were carried out with a spiral-wound Filmtec SW30-2521 membrane (area of 1.19 m²) at a feed water temperature of 28°C–30°C. The concentrate recycle technique was used, in which the permeate stream was withdrawn from the system and the concentrate solution was recycled back to the feed tank (Fig. 1). The concentrate flow rate in all runs was kept constant at 500 L/h. Permeate withdrawal leads to a gradual increase in the concentration of the feed water, simulating the changes along the membranes in a real system. The concentration effect induces a continuous increase in the scaling potential in the system. A maximum limiting water recovery fraction characterizing the antiscalant (AS) performance was detected by a rapid drop in the membrane permeability (i.e., permeate flux) [11,12]. A feed solution volume of 200 L was used in order to provide an adequate inventory of scaling material in the feed solution. This ensures that there is sufficient scaling material to clog the membrane to a degree that can be conveniently detected by permeability decline measurements.

At the beginning of each experiment, the membrane permeability was determined by deionized water tests to ensure that the membrane was undamaged by previous experiments. At the termination of each experiment, the membrane was cleaned with citric acid (2% wt.). All experiments were conducted at least in duplicates.

2.2. Feed water and AS

Experiments were conducted using synthetic solutions simulating brackish water fed to a desalination plant in southern Israel which requires $CaCO_3$ scale control. The solution was prepared by dissolving NaCl, $CaCl_2·2H_2O$, $NaHCO_3$, $MgCl_2·6H_2O$, $MgSO_4·7H_2O$, and $Na_2O_3Si·5H_2O$ salts in 200 L of deionized water. The solution pH was adjusted to 7.1–7.2 by bubbling CO_2 into the feed solution. Table 1 displays the
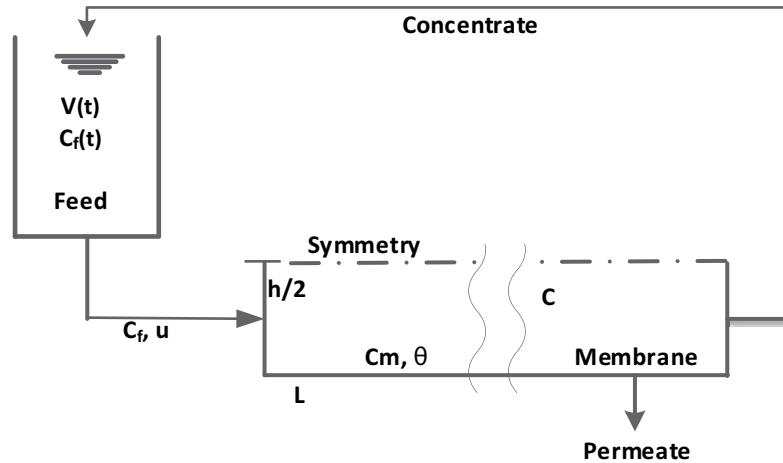
Fig. 1. Schematics of the concentrate recycle system two-dimensional computational fluid dynamics model. The feed solution enters the space of thickness *h* between two reverse osmosis membranes. The permeate exits the system and the concentrate is recycled back to the feed tank.

Table 1
Composition of feed solution

Species	mg/L
Ca^{2+}	105
Mg^{2+}	80
Na^+	365
SO_4^{2-}	90
HCO_3^-	405
Cl^-	650
SiO_2	27
TDS	1,810
pH	7.1–7.2

composition of this solution and Table 2 lists the polycarboxylate AS tested.

The supersaturation index (SI) is defined by the saturation ratio presented in Eq. (1). Assuming 100% rejection, the SI of calcite in the bulk solution (SIb) was calculated using Visual MINTEQ V. 3.1. The SI of calcite is presented as this is the major crystal form of calcium carbonate formed on RO membranes. This is due to its high thermodynamic stability and low solubility [20]. The highest SI is maintained on the membrane surface (denoted as SI_m) due to the concentration polarization effect. The calcite supersaturation level on the membrane surface is given by Eq. (2).

$$SI_b = \frac{\{Ca^{2+}\} \cdot \{CO_3^{2-}\}}{K_{sp}} \tag{1}$$

where K_{sp} is the solubility product of calcite.

$$SI_m = SI_b \left(CP^2 \right) \tag{2}$$

where CP is the concentration polarization [Eq. (3)] calculated by the ratio between the solute concentrations at the membrane surface (C_m) and at the bulk (C_b).

Table 2
Inhibition grading of the tested polycarboxylate AS according to the manufacturer

Antiscalant	$CaCO_3$ inhibition
AS-B	Excellent
AS-C	Excellent
AS-D	Good
AS-E	Good

$$CP = \frac{C_m}{C_b} = \exp\left(\frac{J_v}{k_D}\right) \tag{3}$$

where J_v is the permeate flux and k_D is the mass transfer coefficient [Eq. (4)] [21].

$$k_D = \frac{\left(J_v\right)_{Salt}}{\ln\left\{\frac{\Delta P}{\pi_b} \cdot \left[1 - \frac{\left(J_v\right)_{Salt}}{\left(J_v\right)_{Water}}\right]\right\}} \tag{4}$$

where ΔP is the hydraulic pressure differential across the membrane and π_b is the osmotic pressure of the bulk solution.

Experimental determination of the CP at the concentrate flow rate of 500 L/h and inlet pressures of 20 and 30 bar (net driving pressures (NDP) of 19.0 and 28.5 bar, respectively) maintained in all tests yielded values of CP = 1.20 and 1.42, respectively. The concentrations of calcium ions was determined using EDTA titrimetric method (Standard Methods 2340C) [22].

3. Model development

For the model development and for simulation of the experimental results, COMSOL 5.2a software was used. The solution flow was simulated by the stationary laminar flow module. Solute concentration in the feed solution was

simulated by the time-dependent convection and diffusion module, taking into account the continuous increase of the feed concentration, $C_f(t)$, due to the permeate withdrawal (Fig. 1). The CaCO$_3$ scaling on the membrane surface was simulated by the time-dependent surface reaction module. The coupling of the three modules was done as follows: (i) the velocity field derived by the flow module was used as an input to the convection and diffusion module; (ii) the concentration on the membrane surface (C_m), derived by the convection and diffusion module, was used as an input to the surface reaction module for simulating the scaling surface coverage θ. Input constants, based on the experimental conditions, are listed in Table 3. The data sets differ by the concentration of the antiscalants (0, 2 and 4 mg/L) and applied pressure (20 and 30 bar).

The solution flow rate Q_f enters the space between the two membranes of the flow module at pressure p and leaves the concentrate side at p–1. The permeate flux J_v and permeate flow rate Q_p is given by Eqs. (5) and (6).

$$J_v = L_p (\Delta p - \Delta \pi) \tag{5}$$

$$Q_p = J_v A_m (1 - \theta) \tag{6}$$

where L_p is the membrane permeability (m/s·Pa); ΔP is the hydraulic pressure differential across the membrane (Pa); $\Delta \pi$ is the osmotic pressure differential across the membrane (Pa); the bulk concentration $C_b(x,t)$ at the membrane surface, provided by the convection and diffusion module, varies with x along the membrane and with the operation time $t(\text{p}(C_p))$ was neglected relative to p(C_b); A_m is the membrane area; θ is the scaling coverage fraction.

The convection part of the module is the velocity field developed by the flow module. The concentrate recycling technique yields a continuous increase of the feed concentration $C_f(\varphi)$ with the recovery fraction [Eq. (7)] due to the permeate withdrawal and recycle of the concentrate back to the feed tank.

$$\varphi = \frac{V_p}{V_0} \tag{7}$$

Table 3
Constants used as inputs for the computational fluid dynamics simulations

Parameter	Value	Description
A_m	1.19 m²	Membrane area
AS	2 or 4 mg/L	Antiscalant concentration
$C_f(0) = C_0$	105 mg/L	Initial concentration of Ca²⁺ (Table 1)
D_{Ca}	1.31 ′ 10⁻⁹ m²/s	Diffusion coefficient of Ca²⁺ in the solution
h	0.66 mm	Spacer thickness
L	432 mm	Membrane length
P	20 or 30 bar	Applied pressure
Q_f	540 L/h	Feed flow rate

where φ is the water recovery fraction V_0 is the initial solution volume in the feed tank (L), and V_p is the permeate volume withdrawn from the system (L).

Since the inlet concentration in the COMSOL software is time-dependent, the experimental φ should also be time-dependent. With the measured permeate flow rate $Q_p(\varphi)$ Eq. (8) provides required conversion of φ to t.

$$t(\varphi) = V_0 \int_0^\varphi \frac{dx}{Q_p(x)} \tag{8}$$

Deposition and removal of scalants on and off the membrane surface, respectively, result in a net CaCO$_3$ scaling flux F_{sc} (mol/m²·s). The net scaling flux exits the bulk to the membrane surface as follows:

$$F_{sc} = r_a - r_d, \quad r_a = k_a C_m \quad \text{and} \quad r_d = k_d \theta, \quad \theta = \frac{C_s}{C_{sm}} \tag{9}$$

where r_a and r_d are the scale deposition and removal rates, respectively (mol/m²·s), k_a is the deposition rate coefficient (m/s); k_d is removal rate coefficient (mol/m²·s); C_m is the concentration at the membrane surface (mol/m³), C_s is the scale surface concentration (mol/m²), and C_{sm} is the maximum surface concentration (mol/m²).

The surface coverage fraction θ(t) was derived by solving the surface reaction module for the initial value θ(0) = 0. The maximum surface concentration $C_{sm} = 5 \times 10^{-4}$ mol/m² was determined by fitting Eq. (6) to the experimental Q_p. The adjustable parameter k_a was extracted by fitting the CFD model to the experimental data of the permeate flux vs. time.

The main assumption underlying the model is that there are two distinct flux decline regimes induced by the permeate withdrawal, one due to the osmotic pressure increase in a concentrating solution and the other due to scale-mass growth. These regimes, which are separated by the onset of scaling, are well manifested by the real membrane permeability (Section 4.2 – Membrane scaling). The decrease in flux prior to the onset of scaling is primarily caused by an increase in osmotic pressure. Beyond the onset of scaling, scale-mass growth is the dominant cause of permeate flux decline. For $t < \tau_{os}$ (i.e., time of onset of scaling), it is assumed that there is a constant balance between CaCO$_3$ particles deposition and dissociation. For $t > \tau_{os}$, the effect of dissociation diminishes dramatically in comparison to scale-mass growth. These considerations are expressed mathematically for k_d in Eq. (10). The scaling rate coefficient (k_a) and the time of onset of scaling (τ_{os}) are adjustable parameters of the model for each data set.

$$k_d = 5.1 \times 10^{-6}, \ t < \tau_{os}; \ k_d = 5.1 \times 10^{-6} \exp\left(-3.95 \frac{t}{\tau_{os}}\right), \ t \geq \tau_{os} \tag{10}$$

4. Results

4.1. Bulk precipitation

Control experiments consisted of runs performed without antiscalant dosage to provide a reference to the scaling

propensity of the tested solution. Fig. 2 displays the observed changes in the various scale-indicating parameters, including turbidity, pH, calcium concentration, and permeate flux, for duplicate experiments denoted by the run number C1 and C2. As seen in Fig. 2, very good agreement was obtained between the duplicate experiments.

Cumulative evidence from the experimental data indicated that the onset of scaling occurred at a water recovery fraction close to 0.65. Precipitation occurred in the bulk solution, as evident by a sharp increase in the feed solution turbidity to a value above 100 NTU (Fig. 2a). This observation was supported by a sharp decrease in the feed solution pH (Fig. 2b), and by the calcium analysis (Fig. 2c), which revealed a deviation between the measured and theoretical concentrations, based on the concentration factor and rejection of the membrane. The permeate flux decline (Fig. 2d) is attributed mainly to the increased osmotic pressure, yet it is possible that $CaCO_3$ particles formed in the bulk solution precipitated on the membrane hence, affected the permeate flux. Bulk precipitation of $CaCO_3$ was also obtained for AS-D and AD-E at a dosage of 2 mg/L (data not shown).

4.2. Membrane scaling

Typical results of the permeate flux decline and membrane permeability are displayed Fig. 3. As explained earlier, the decline in permeate flux is caused by both scale precipitation and an increase in osmotic pressure due to the concentration of the feed solution caused by the permeate withdrawal and recycling of the concentrate. Therefore, a continuous decline of the permeate flux is obtained as the water recovery fraction is increased. The flux decline can be divided into two parts, transitioning at the onset of scaling as indicated by the red circle in Fig. 3a. The first part, up

to a water recovery fraction of 0.75, corresponds to a slow permeate flux decline predominantly controlled by the increased osmotic pressure. In the second part, $\varphi > 0.75$, a sharp decline is observed, which can be attributed to the growth of the scale mass (Fig. 3a).

The pure effect of scaling can be obtained by obstructing the effect of osmotic pressure. Hence, scaling is detected from the "real" membrane permeability L_p, given by Eq. (11). A decline in the real permeability is detected when a sufficient membrane area is obstructed by a scale deposit. In the absence of sufficient scale deposition, $L_p = L_{p0}$ at increasing water recovery fractions, where L_{p0} denotes the intrinsic membrane permeability of a clean, un-scaled membrane, as seen in Fig. 3b. Therefore, the observed onset of scaling is determined by the last measured point before the sharp permeability decline, $\varphi = 0.8$, marked with an arrow in Fig. 3b.

$$L_P = \frac{J_V}{(\Delta P - \pi_m)} = \frac{J_V}{(\Delta P - CP \cdot \pi_b)} \tag{11}$$

where, π_m is the osmotic pressure on the membrane surface which can be evaluated from the solution bulk osmotic pressure π_b, and the CP level.

4.3. Replicability of the experimental results

In this section, the replicability of four experiments conducted at an NDP of 28.5 bar with a dosage of 4 mg/L of AS-E, denoted AS-E RR1 through RR4 in Table 4 are quantified. The repeatability of the permeate flux and membrane permeability is illustrated in Fig. 4. As seen, the reproducibility of both parameters was very good, with an error ≤3.5% and 2.8% for the permeate flux and membrane permeability, respectively.
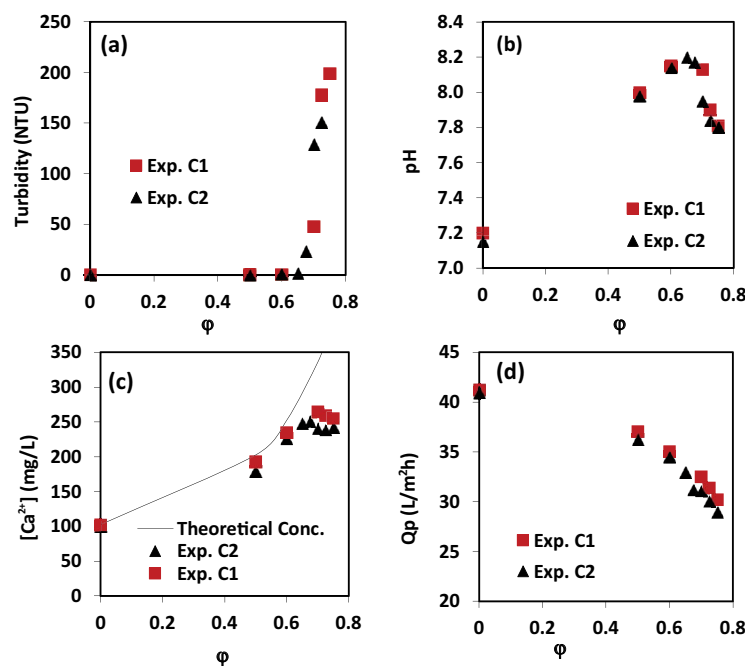
Fig. 2. Observed changes in (a) turbidity, (b) pH, (c) calcium concentration, and (d) permeate flux as a function of the water recovery fraction (without dosage of AS).
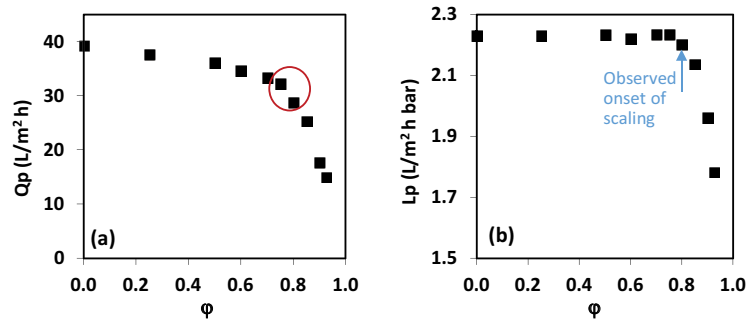
Fig. 3. (a) Permeate flux and (b) real membrane permeability as a function of the water recovery fraction (2 mg/L AS-B, 19 bar).

Table 4
Deposition rate coefficients, water recovery fraction, surface coverage, and saturation indices at the onset of $CaCO_3$ scaling with a dosage of antiscalants

AS	AS dosage (mg/L)	NDP (bar)	k_a (nm/s)	φ_{os}	$\theta@0.9\ \varphi_{os}$	SI_b	SI_m
						@onset of scaling	
AS-B	2	19.0	4.0	0.814	0.0679	2.52	3.65
AS-C	2	19.0	4.0	0.829	0.0082	2.58	3.73
AS-D R1	4	19.0	13.0	0.822	0.0261	2.55	3.69
AS-D R2	4	19.0	16.0	0.870	0.0320	2.74	3.97
AS-D R3	4	19.0	14.0	0.814	0.0256	2.52	3.65
AS-E R1	4	19.0	6.0	0.761	0.0223	2.32	3.35
AS-E R2	4	19.0	8.7	0.748	0.0175	2.27	3.28
AS-E RR1	2	28.5	8.7	0.769	0.0175	2.35	4.73
AS-E RR2	2	28.5	7.9	0.725	0.0169	2.18	4.40
AS-E RR3	2	28.5	7.6	0.733	0.0144	2.21	4.46
AS-E RR4	2	28.5	9.0	0.725	0.0198	2.18	4.40
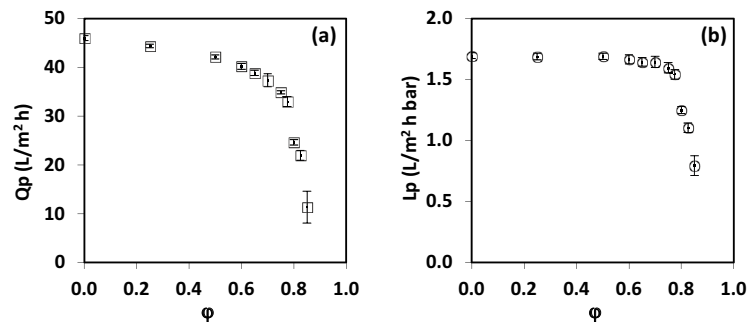
Fig. 4. (a) Permeate flux and (b) membrane permeability as a function of the water recovery fraction. Data points represent the average of the four repeated experiments (4 mg/L AS-E at 28.5 bar) with the standard deviations shown by the error bars.

It is important to note that the experimental onset of scaling was determined based on the degree of membrane clogging detected by permeate flux decline measurements. Thus the slope in Fig. 4 reflects the growth of the $CaCO_3$ layer on the membrane surface. In the scaling process, initially nano-sized nuclei are formed once supersaturation conditions are attained, after which they grow into crystals of micrometer size, that cover the membrane surface. The growth rate of this scale depends mainly on solution supersaturation, temperature, and Reynolds number. therefore, differences in the permeate flux decline/membrane permeability are expected.

4.4. Model fitting to the experimental results

Fitting the CFD model to the experimental data enables the simulation of the distribution of calcium concentration in the bulk and on the membrane surface over time and space

between the two symmetric membranes (Fig. 1) to follow the scale development. Each experiment provided the calcium feed concentration C_f and the permeate flow rate $Q_p(\varphi)$ as a function of the water recovery φ. Two of the COMSOL modules, namely convection and diffusion, and surface reaction, are time-dependent. Therefore, as explained in Section 3 – Model development, $Q_p(\varphi)$ was converted to $Q_p(t)$ according to Eq. (8), to obtain $\varphi(t)$ and $C_f(\varphi(t))$ or $C_f(t)$. The resulting $C_f(t)$ was then used as the feed concentration as feed concentration for the model.

A fit of the model to an experimental data set was obtained by adjusting the deposition rate constant, k_a [Eq. (10)], and the water recovery fraction at the onset of scaling, φ_{os}. Typical fits of the model to the experimental data are shown in Fig. 5, with the onset of scaling indicated by arrows. As seen in Fig. 5, a good fit between the model and the experimental data was obtained, validating the model at different dosages of antiscalants and applied pressures.

The k_a, φ_{os}, surface coverage (θ) at 0.9 φ_{os}, and saturation indices (SI_b and SI_m) at the onset of scaling are listed in Table 4. The derived values of k_a ranged between 4 and 16 nm/s. Higher values were obtained for 4 mg/L of antiscalant and a net driving pressure of 28.5 bar as compared
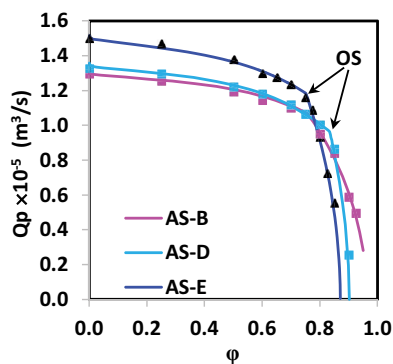
to 2 mg/L and 19 bar, respectively. The difference between the k_a values of replicated experiments ranged from 10.6% for AS-D to 6.2 and 7.2% for AS-E at 19.0 and 28.5 bars, respectively. The differences are due to the deviation in the slope after the onset of scaling.

An average value of φ_{os} = 0.830±0.023 water recovery fraction was obtained at a NDP of 19.0 bar, with AS-B and AS-C at a dosage of 2 mg/L and AS-D at a dosage of 4 mg/L. AS-E exhibited less efficient inhibitory performance, obtaining a 10% lower water recovery fraction of 0.745 ± 0.019 at a dosage of 4 mg/L and net driving pressures of 19.0 and 28.5 bar.

The degree of the scale coverage is controlled by the number of surface crystals nucleating on the membrane surface and their growth rate [23]. As seen in Table 4 the membrane surface coverage at 0.9 φ_{os} ranges between 0.8 and 3.2% of the membrane surface. The coverage was calculated at 0.9 φ_{os} of the onset of scaling, to avoid the possible effect of the sharp decrease in the permeate flux at the onset of scaling. It should be noted that φ_{os} may be used as a reference point to determine practical desalination water recovery before scaling affects the permeate flux.

Another performance indicator evaluated from the tests was the $CaCO_3$ supersaturation level in the bulk solution and on the membrane surface at the onset of scaling. As seen in Table 4, the SI_b levels at the onset of scaling differ slightly, exhibiting a mean value of SI_b = 2.40 ± 0.188. As the SI_m is dependent on the concentration polarization [Eq. (2)], values of 3.62 ± 0.228 and 4.50 ± 0.157 were obtained for NDP of 19.0 and 28.5 bars, respectively. The close proximity of the values, within 6.3% error, obtained for the different antiscalants (NDP = 19 bar) confirms that the main criterion for the onset of scaling is the supersaturation level reached, and that an increase in antiscalant dosage only slightly augments the scaling limits.

4.5. Spatial and temporal distribution of calcium bulk concentration

Color maps of the distribution of bulk calcium concentration along the membrane and as a function of the water recovery fraction are displayed in Fig. 6. Similar to once-through

Fig. 5. Typical fits of the model (lines) to the experimental data (symbols) using AS-B (2 mg/L, 19.0 bar), AS-D (4 mg/L, 19 bar) and AS-E (4 mg/L, 28.5 bar).
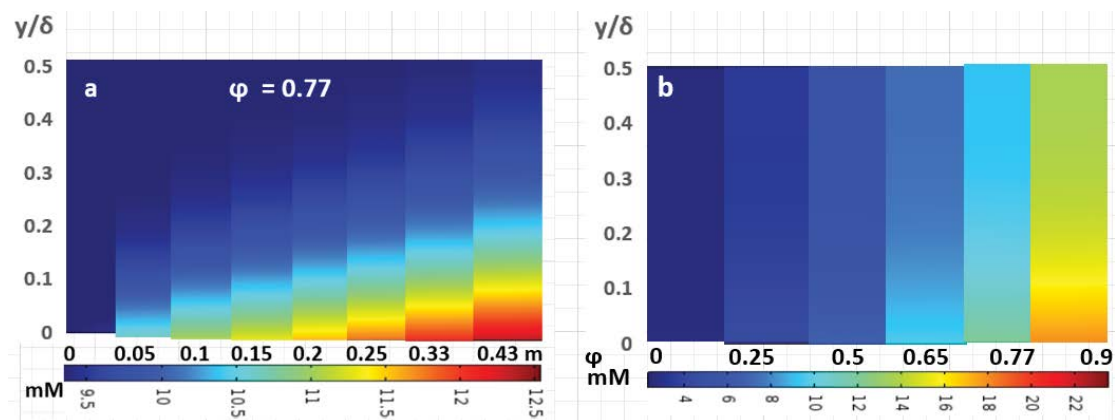
Fig. 6. Color maps of the concentration distribution of calcium (a) half-symmetric two-dimensional bulk flow area of one of the two symmetric membranes as a function of the membrane length; φ = 0.77 was chosen for more colorful illustration and (b) distribution of half-symmetric calcium concentrations as a function of water recovery fraction at membrane exit. For both (a) and (b) the vertical axis is the half spacer thickness $\delta/2$.
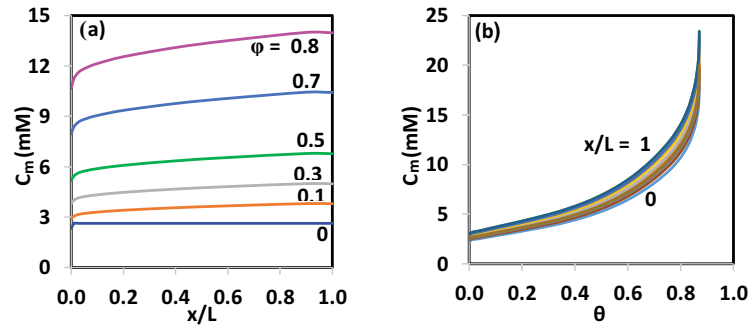
Fig. 7. Development of C_m (a) along the membrane at various water recovery fractions and (b) as a function of the water recovery fraction at various points along the membrane (4 mg/L AS-E at NDP = 19 bar).
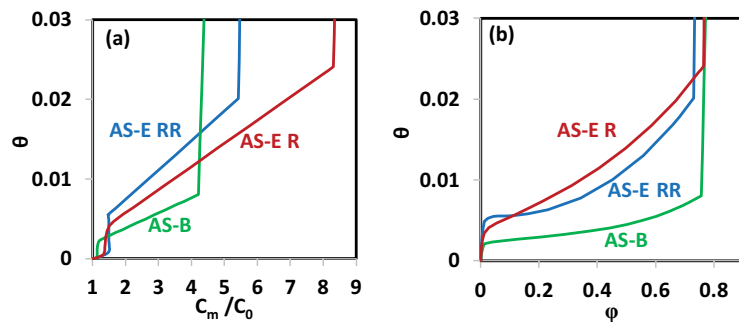
Fig. 8. Development of membrane surface coverage as a function of (a) concentration at the membrane surface and (b) water recovery fraction. The sharp increase of θ indicates the transition from crystallization to scale-mass growth stages.

reverse osmosis, in the concentrate recycle technique, the bulk calcium concentration gradually increases along the length of the membrane (Fig. 6a). The concentration is lowest at the entrance of the membrane and gradually increases towards the downstream end. concentration polarization results in a higher concentration near the membrane surface. As expected, the bulk calcium concentration increases with the water recovery fraction (Fig. 6b).

4.6. Distribution of the membrane surface concentration

Despite the approach to real-time analysis of mineral scale formation on reverse osmosis membranes [24], the model presented herein enables the derivation of the concentration of the solute at the membrane surface (C_m) and the buildup of the membrane surface coverage fraction (θ). The good fit of the model to the experimental data yielded values of C_m and θ as displayed in Fig. 7. As seen in the Fig. 7, C_m increases continuously with both the water recovery fraction and along the membrane. Due ro concentration polarization $C_m > C_f(\varphi)$ at the membrane surface. At $x = 0$, $C_m = C_f(\varphi)$. Following the onset of scaling, C_m increases sharply ($\varphi > 0.8$).

4.7. Membrane surface coverage

The net scaling is determined by the mass balance between two simultaneous and opposing transport processes: deposition to and removal from the membrane surface [10]. When the deposition rate is greater than the removal rate, membrane scaling occurs. Fig. 8 displays the

development of membrane surface coverage as a function of the normalized solute concentration at the membrane surface (C_m/C_0) and as a function of the water recovery fraction. The C_m values in Fig. 8 were normalized to the initial concentration C_0 to better reflect the trends. As seen in Fig. 8a, the membrane coverage fraction θ increases linearly with $C_m/C_0 > 1.4$ for AS-B and 1.6 for AS-E until it reaches the onset of scaling ($C_{m,os}$). The onset of scaling clearly distinguishes between the predominant CaCO$_3$ removal from the membrane surface and the dominant deposition on it, as described by Eq. (10). Beyond the onset of scaling, a sharp increase in surface coverage is observed, resulting in a sharp flux decline [8]. The competition between deposition and removal rates results in small net scaling with a membrane surface coverage θ of 1% or $C_s = 5 \times 10^{-6}$ mol/m^2 for C_m lower than $C_{m,os}$. Beyond the onset of scaling, the θ increases sharply, indicating CaCO$_3$ scale-mass growth. Similar trends in the surface coverage as a function of the water recovery fraction are shown in Fig. 8b. Since Fig. 8a and 8b represent the overall effects of the operating condition, water quality, and antiscalant dosages, they can be used to determine the best conditions to achieve the highest water recovery fraction without reaching the onset of scaling.

5. Concluding remarks

A CFD model was developed to analyze the effect of continuously increasing CaCO$_3$ scaling potential on the scaling of RO membranes. The model couples flow convection and diffusion modules with the surface reaction module

of COMSOL 5.2a software. It accounts for two flux decline regimes: a slow flux decline up to the onset of scaling caused by continuous osmotic pressure increase, and a sharp flux decline beyond the onset of scaling caused by scale-mass growth.

The onset of scaling was experimentally determined by the permeate flux decline, which showed excellent replicability. The model was fit to the experimental results to yield a pair of parameters: the deposition rate and the water recovery fraction at the onset of scaling. With these two adjustable parameters, the model generates concentration profiles of calcium in the bulk solution and on the membrane surface as a function of the water recovery fraction and along the membrane length.

The model also provided the membrane surface coverage fraction, which increases with C_m up to the onset of scaling. At this point, it was in the order of 0.01, with the scale surface concentration of around 5×10^{-6} mol/m^2. The saturation indices at the onset of scaling, at a given NDP, were in close proximity for all antiscalants tested. This confirms that the main criterion for the onset of scaling is the level of supersaturation reached.

Overall, the model presented in this paper enables to simulate the bulk and membrane solute concentrations for a given system as well as the CaCO$_3$ scale development on the membrane under various desalination conditions. Therefore, it can be used to aid in selecting operating conditions and antiscalant dosage to achieve maximum water recovery without reaching the onset of scaling.

References

[1]   W. Yu, D. Song, W. Chen, H. Yang, Antiscalants in RO membrane scaling control, Water Res., 183 (2020) 115985, doi: 10.1016/j.watres.2020.115985.

[2]   A. Matin, F. Rahman, H.Z. Shafi, S.M. Zubair, Scaling of reverse osmosis membranes used in water desalination: phenomena, impact, and control; future directions, Desalination, 455 (2019) 135–157.

[3]   J. Rolf, T. Cao, X. Huang, C. Boo, Q. Li, M. Elimelech, Inorganic scaling in membrane desalination: models, mechanisms, and characterization methods, Environ. Sci. Technol., 56 (2022) 7484–7511.

[4]   Q. Liu, G.-R. Xu, R. Das, Inorganic scaling in reverse osmosis (RO) desalination: mechanisms, monitoring, and inhibition strategies, Desalination, 468 (2019) 114065, doi: 10.1016/j.desal.2019.07.005.

[5]   A.J. Karabelas, S.T. Mitrouli, M. Kostoglou, Scaling in reverse osmosis desalination plants: a perspective focusing on development of comprehensive simulation tools, Desalination, 474 (2020) 114193, doi: 10.1016/j.desal.2019.114193.

[6]   A. Antony, J.H. Low, S. Gray, A.E. Childress, P. Le-Clech, G. Leslie, Scale formation and control in high pressure membrane water treatment systems: a review, J. Membr. Sci., 383 (2011) 1–16.

[7]   S. Lee, C.H. Lee, Scale formation in NF/RO: mechanism and control, Water Sci. Technol., 51 (2005) 267–275.

[8]   H.-J. Oh, Y.-K. Choung, S. Lee, J.-S. Choi, T.-M. Hwang, J.H. Kim, Scale formation in reverse osmosis desalination: model development, Desalination, 238 (2009) 333–346.

[9]   W. Wei, X. Zou, X. Ji, R. Zhou, K. Zhao, Y. Wang, Analysis of concentration polarisation in full-size spiral wound reverse osmosis membranes using computational fluid dynamics, Membranes (Basel), 11 (2021) 353, doi: 10.3390/membranes11050353.

[10] A. Sagiv, X. Li, R. Semiat, H. Shemer, Theoretical tool for evaluating induction periods of calcium sulfate scaling on reverse osmosis membranes, Desal. Water Treat., 258 (2022) 64–71.

[11] A. Drak, K. Glucina, M. Busch, D. Hasson, J.-M. Laîne, R. Semiat, Laboratory technique for predicting the scaling propensity of RO feed waters, Desalination, 132 (2000) 233–242.

[12] D. Hasson, A. Drak, R. Semiat, Inception of CaSO$_4$ scaling on RO membranes at various water recovery levels, Desalination, 139 (2001) 73–81.

[13] R. Semiat, I. Sutzkover, D. Hasson, Technique for evaluating silica scaling and its inhibition in RO desalting, Desalination, 140 (2001) 181–193.

[14] D. Hasson, A. Drak, R. Semiat, Induction times induced in an RO system by antiscalants delaying CaSO$_4$ precipitation, Desalination, 157 (2003) 193–207.

[15] D. Hasson, S. Rachamim, R. Semiat, Effect of concentrate recycle on antiscalant performance, Desal. Water Treat., 6 (2009) 18–24.

[16] A.J. Karabelas, S.T. Mitrouli, C.P. Koutsou, M. Kostoglou, Prediction of spatial-temporal evolution of membrane scaling in spiral wound desalination modules by an advanced simulator, Desalination, 458 (2019) 34–44.

[17] W. Li, X. Su, A. Palazzolo, S. Ahmed, Numerical modeling of concentration polarization and inorganic fouling growth in the pressure-driven membrane filtration process, J. Membr. Sci., 569 (2019) 71–82.

[18] A.I. Radu, L. Bergwerff, M.C.M. van Loosdrecht, C. Picioreanu, A two-dimensional mechanistic model for scaling in spiral wound membrane systems, Chem. Eng. J., 241 (2014) 77–91.

[19] W. Mao, X. Zou, Z. Guo, S. Sun, S. Ma, S. Lyv, Y. Xiao, X. Ji, Y. Wang, Numerical simulations of calcium sulfate scaling in full-scale brackish water reverse osmosis pressure vessels using computational fluid dynamics, Membranes (Basel), 11 (2021) 521, doi: 10.3390/membranes11070521.

[20] K.-G. Lu, H. Huang, M. Li, Reverse Osmosis Membrane Scaling During Brackish Groundwater Desalination, H.-H. Tseng, W.J. Lau, M.A. Al-Ghouti, L. An, 60 Years of the Loeb-Sourirajan Membrane: Principles, New Materials, Modelling, Characterization, and Applications, Elsevier, 2022, pp. 603–626. https://doi.org/10.1016/B978-0-323-89977-2.00010-5

[21] I. Sutzkover, D. Hasson, R. Semiat, Simple technique for measuring the concentration polarization level in a reverse osmosis system, Desalination, 131 (2000) 117–127.

[22] Standard Methods for the Examination of Water and Wastewater, American Public Health Association/American Water Works Association/Water Environment Federation, 21st ed., Washington, D.C., USA, 2005.

[23] M. Uchymiak, E. Lyster, J. Glater, Y. Cohen, Kinetics of gypsum crystal growth on a reverse osmosis membrane, J. Membr. Sci., 314 (2008) 163–172.

[24] A.R. Bartman, E. Lyster, R. Rallo, P.D. Christofides, Y. Cohen, Mineral scale monitoring for reverse osmosis desalination via real-time membrane surface image analysis, Desalination, 273 (2011) 64–71.